

Prospects for a neutron EDM measurement with an advanced ultracold neutron source at TRIUMF

Takashi Higuchi^{1,*} on behalf of the TUCAN collaboration

¹Research Center for Nuclear Physics, Osaka University,
10-1 Mihogaoka, Ibaraki, Osaka 567-0047, Japan

Abstract. The TUCAN (TRIUMF Ultra-Cold Advanced Neutron) collaboration is building a new high-intensity ultracold neutron (UCN) source at TRIUMF with the aim of measuring the neutron electric dipole moment (nEDM) with unprecedented precision. TUCAN employs a spallation-driven superthermal UCN production scheme which has been demonstrated with a prototype UCN source. In this article, recent progress on the major components of a new upgraded UCN source and developments in the context of installation of the nEDM spectrometer are reported.

1 Introduction

1.1 Background

Tests of discrete symmetries have occupied an important place in modern particle physics since parity (P) violation in the weak interaction was first discovered [1, 2]. In 1967, Sakharov proposed a scenario for explaining the baryon-antibaryon asymmetry of the universe based on a few fundamental conditions, including Charge-Parity (CP) violation [3]. The baryon asymmetry η of the current universe is defined as

$$\eta = \frac{n_B - n_{\bar{B}}}{n_\gamma}, \quad (1)$$

with $n_B, n_{\bar{B}}$ and n_γ being the number densities of baryonic matter, antibaryonic matter and photons, respectively. Based on CP violation of the Standard Model (SM), η is predicted to be $\eta_{\text{SM}} \sim 10^{-20}$ [4]. However, $\eta_{\text{obs}} \sim 10^{-10}$ is found from observation of the cosmic microwave background [5], revealing a severe deficit of the SM in explaining the observed matter abundance of the universe. This motivates searches of undiscovered sources of CP violation, spanning different sectors of particle physics today [6–8].

A non-zero value of the electric dipole moment (EDM) of a non-degenerate system, such as the neutron, would violate time-reversal (T) symmetry. This is equivalent to CP violation, assuming the CPT theorem [9] fundamental to relativistic quantum field theories. EDMs have been searched in different physical systems, such as the neutron, the electron and atoms [8], however no finite EDM has ever been observed. They have complementary sensitivities to undiscovered sources of CP violation, which would manifest differently in the different systems. Effective field theories provide a framework to interpret the experimental limits and

*e-mail: thiguchi@rcnp.osaka-u.ac.jp

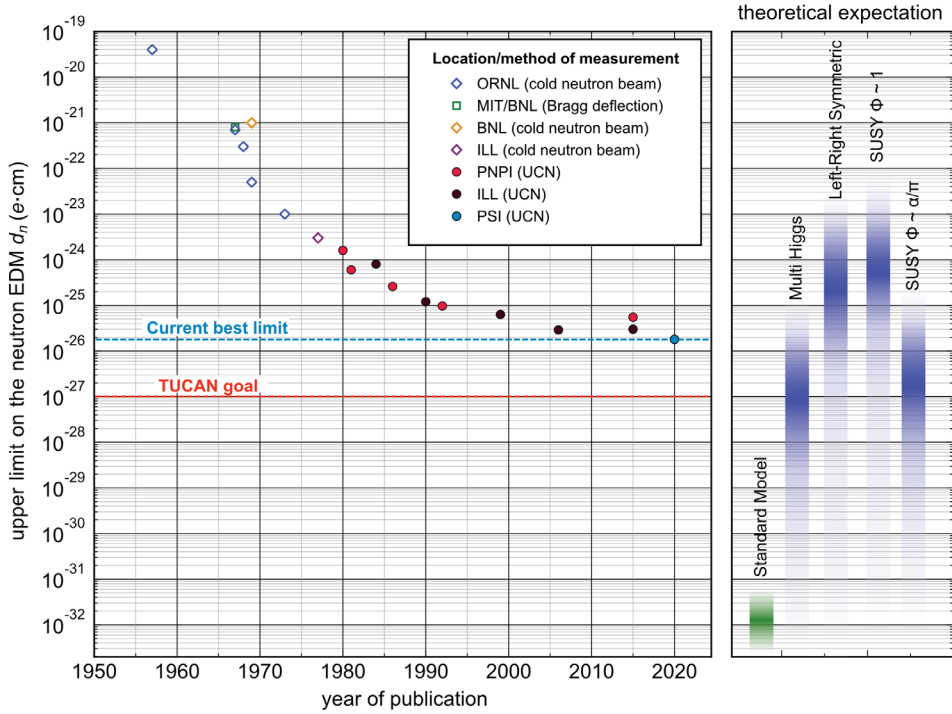


Figure 1. Historical development of the experimental upper limit on the nEDM. The method and the location of the experiments are indicated in the legend. The theoretical predictions according to the SM and BSM theories are shown on the right. The SM expectation is based on Ref. [8]. The expected values from the BSM models are based on Ref. [11].

place stringent constraints on super-symmetry models and other theories beyond the Standard Model [10].

In Fig. 1, development of the experimental upper limit on the neutron EDM (nEDM) over time is plotted together with theoretical expectations. The prediction based on SM CP violation is on the order of $10^{-32} e \cdot \text{cm}$. On the other hand, the BSM theories expect orders of magnitude larger nEDM, which could be in reach of future experiments. The experimental method and the location of each measurement are indicated in the legend. Since the first direct measurement by Smith, Purcell and Ramsey [12] until a result obtained in 1977 [13], beams of cold neutrons were used. Since the 1970s, ultracold neutrons (UCNs) have been used for nEDM measurements, enabling the experimentalists to reach a precision on the order of $10^{-26} e \cdot \text{cm}$. The UCNs refer to neutrons with kinetic energies $\lesssim 300$ neV. Because of their extremely low energies, UCNs are totally reflected on appropriately-chosen material surfaces. As the consequence, they can be stored in a measurement volume for times on the order of 100 s, which greatly benefits the statistical sensitivity of the nEDM measurements. Such stored UCNs are also used at an experiment at PSI where the current best limit was obtained [14].

The major limiting factor of recent nEDM measurements is the number of UCNs available for the measurements, which is typically on the order of $N \sim 10^4$ per cycle. Therefore, an intense UCN source is one of the keys for a further development in the field.

1.2 The TRIUMF Ultra-Cold Advanced Neutron collaboration

The international TUCAN (TRIUMF Ultra-Cold Advanced Neutron) collaboration was formed with the aims to build a high-intensity UCN source at TRIUMF and to measure the nEDM with $10^{-27} e \cdot \text{cm}$ precision, thus to improve the current limit by an order of magnitude.

The principle of nEDM measurement is based on spin-precession frequency measurement under a weak ($\sim \mu\text{T}$) magnetic field \mathbf{B} and a strong ($\sim 10 \text{ kV/cm}$) electric field \mathbf{E} . The interaction of the magnetic moment μ_n and the EDM d_n of the neutron with the external fields is represented by a Hamiltonian

$$H = -\mu_n \cdot \mathbf{B} - d_n \cdot \mathbf{E}. \quad (2)$$

To extract the value of d_n , the spin-precession frequencies are compared between configurations where the electric and the magnetic fields are parallel ($\uparrow\uparrow$) and anti-parallel ($\uparrow\downarrow$) to each other. Denoting these frequencies as $\omega_{\uparrow\uparrow}$ and $\omega_{\uparrow\downarrow}$, respectively, d_n can be expressed as

$$d_n = \frac{\hbar(\omega_{\uparrow\uparrow} - \omega_{\uparrow\downarrow})}{4|\mathbf{E}|}. \quad (3)$$

The spin precession frequencies $\omega_{\uparrow\uparrow}$ and $\omega_{\uparrow\downarrow}$ are measured by the Ramsey's technique of separately oscillating fields [15] where two $\pi/2$ pulses separated by a free precession time are used to obtain a spin resonance. In this method, the statistical uncertainty of the nEDM δd_n is determined by the free-precession time T , the number of neutrons N as

$$\delta d_n \sim \frac{\hbar}{|\mathbf{E}|T\sqrt{N}}. \quad (4)$$

Our high-intensity UCN source is expected to provide $N \sim 10^6$ UCNs per cycle to the measurement cell. Together with the other parameters based on realistic assumptions, $|\mathbf{E}| \sim 10 \text{ kV/cm}$ and $T \sim 100 \text{ s}$, $\delta d_n \sim 10^{-25} e \cdot \text{cm}$ per cycle is obtained. The statistical sensitivity goal of $10^{-27} e \cdot \text{cm}$ will be reached in about 400 days of measurement, corresponding to $\sim 10^4$ cycles.

The UCN production scheme of TUCAN was demonstrated with a prototype UCN source operated at TRIUMF in 2017–2019 [18]. Currently, we are building an upgraded UCN source, and in parallel, developing subsystems of the nEDM spectrometer. In the following sections, the UCN production scheme of TUCAN is explained, and some of recent activities towards the planned nEDM measurement with the new UCN source are presented.

2 Provision of Ultracold Neutrons

2.1 Principles of UCN production

The UCN production scheme of TUCAN [19] depicted in Fig. 2 is a combination of spallation neutron production and the super-thermal method using superfluid helium (He-II) [20]. First, a proton beam from an accelerator impinges on a heavy metal target to produce fast neutrons with MeV kinetic energies. They are thermally cooled by layers of neutron moderators to meV energies. The resultant cold neutrons are converted to UCNs via inelastic down-scattering in He-II [20]. The dispersion relation of He-II, as shown in Fig. 3, is characterized by photon and roton excitations. The He-II dispersion curve intersects with that of the free neutron at $\approx 12 \text{ K}$, corresponding to 1 meV . If a neutron with the corresponding momentum enters He-II, it can lose most of its energy by creating one phonon, and be converted to a UCN. After becoming a UCN, it can be guided to a downstream experimental area.

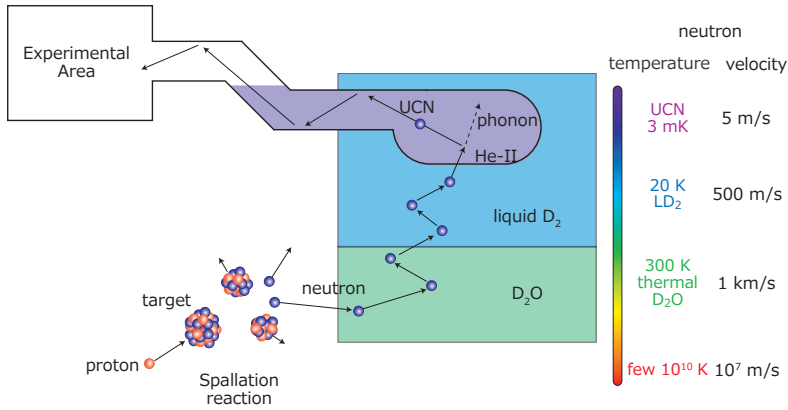


Figure 2. The UCN production scheme of TUCAN. Fast neutrons with MeV energies (corresponding to $\sim 10^{10}$ K temperature) are produced and cooled by a layer of neutron moderators to meV energies (~ 10 K). In a bottle containing He-II, cold neutrons are converted to UCNs and then extracted to the downstream experimental area by reflections inside a UCN guide. Reproduced from Ref. [22].

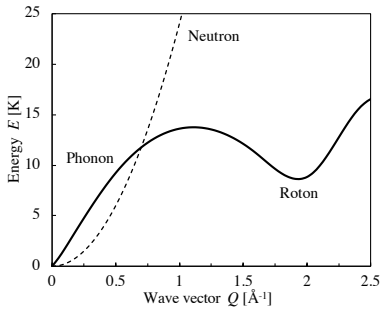


Figure 3. The dispersion curve of phonons and rotons excited in He-II (solid line). It intersects the free neutron curve (dashed line) at a temperature around 12 K. Cold neutrons around this energy are most efficiently converted to UCNs. Adapted from Ref. [16], based on data from Ref. [17].

One of the crucial parameters in this process is the He-II temperature $T_{\text{He-II}}$, because the major UCN loss process is due to heating by up-scattering with phonons, whose rate τ_{up}^{-1} scales as $\tau_{\text{up}}^{-1} \propto T_{\text{He-II}}^7$. For efficient UCN production, $T_{\text{He-II}} \lesssim 1$ K needs to be satisfied. Another important factor is a flux of cold neutrons around the critical energy of 1 meV.

2.2 Achievements with the prototype UCN source

The UCN production method described in the last section was tested with the prototype UCN source, which was originally developed at RCNP, Osaka University and relocated to TRIUMF in 2016. With this prototype source, we succeeded in producing the first UCNs at TRIUMF in 2017 [18]. Results of this beamtime are presented in Fig. 4. Fig. 4a shows typical detector counts. After beam irradiation of the target for 60 s, UCNs stored in the production volume were extracted towards a downstream detector via about 6 m long UCN guides. Shown in Fig. 4b is a relation between the UCN yield and the proton beam current. The UCN yield scales proportionally to the beam current up to $1 \mu\text{A}$. For higher beam currents, however, it drops from this scaling. Under these conditions, temperature increases in the He-II converter were observed. Therefore, the reduction of the UCN yield is due to a heat load on the He-II converter beyond the cooling capacity of the cryostat, which increased the He-II temperature and consequently the up-scattering UCN loss. The prototype source was thus limited by the

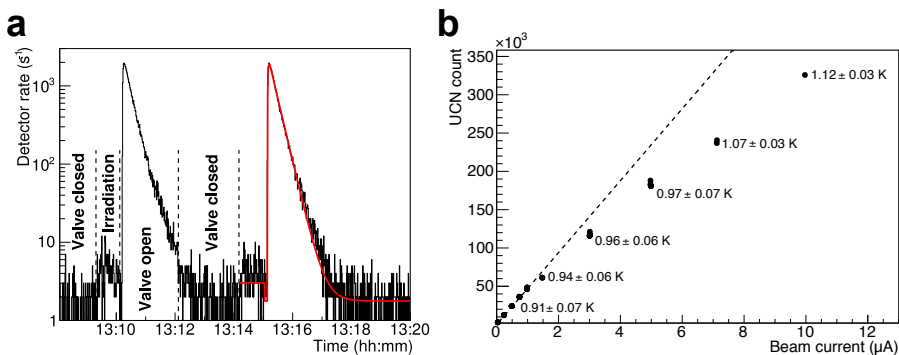


Figure 4. Results obtained during the beamtime 2017 by the prototype UCN source. Reproduced from Ref. [18]. **a.** Detector rate in typical two cycles during operation with a 1 μA beam current. After proton beam irradiation for 60 s, the valve towards the detector is opened for 120 s. While the valve is open, UCNs stored in the irradiation volume are counted by the detector. **b.** The UCN counts extracted from the source after irradiating the spallation target for 60 s with different beam currents. The labels indicate the peak helium temperatures reached under each irradiation condition.

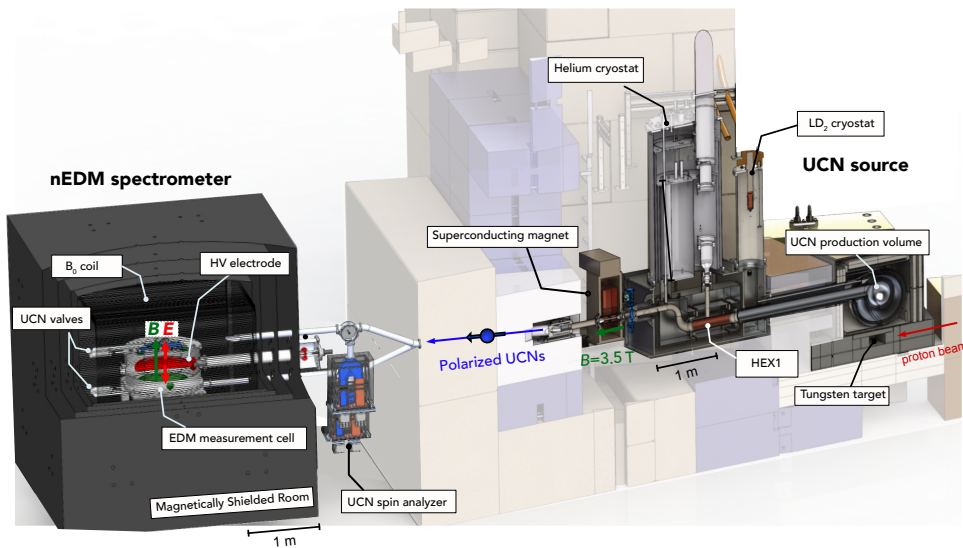


Figure 5. Overview of the new UCN source and the nEDM spectrometer of the TUCAN collaboration. Spallation neutrons from the tungsten target are moderated to cold neutron energies and then converted to UCNs in the production volume filled with He-II. The UCNs are then polarized by a 3.5 T magnetic field of the superconducting magnet and led into the nEDM spectrometer through UCN guides.

cooling power of its cryostat. A typical UCN yield achieved with nominal beam parameters of 483 MeV and 1 μA was 47 500 UCN/cycle for a batch-mode operation with 60 s irradiation, and 1 500 UCN/s in a continuous extraction mode.

2.3 Development of the new UCN source

Based on the experiences with the prototype source, the new UCN source is being developed (Fig. 5), which addresses the limitation of the prototype. The major upgrade is on the helium cryostat [22], which now enables UCN production at 40 μA beam current and increases the

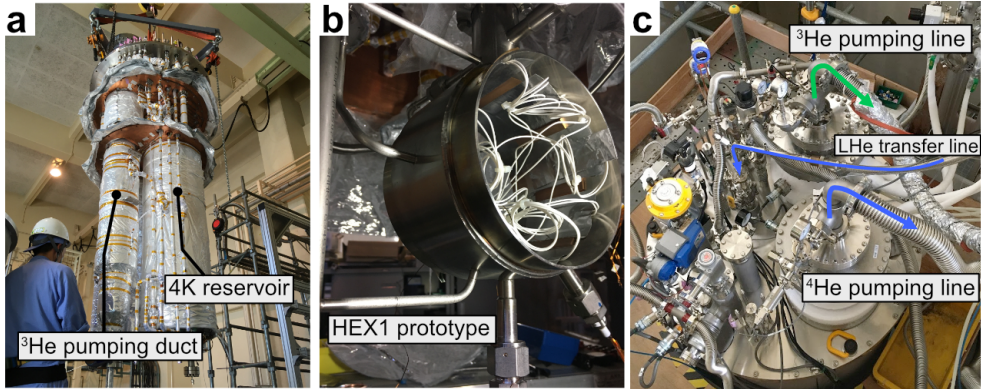


Figure 6. Photographs during the installation of the helium cryostat at KEK for cryogenic tests. For more details of the structure of the cryostat, see Ref. [22]. **a.** The cryostat while the heat shields are being assembled. **b.** The prototype HEX1 attached at the bottom of the cryostat. It has a 1/10 length of the final HEX1 shown in Fig. 5. **c.** The top flange of the cryostat after being installed in a test pit.

UCN yield by a factor of 40. Replacement of the cold-neutron moderator from solid heavy water (sD_2O) to liquid deuterium (LD_2) adds another factor of 3 gain in the UCN yield, because LD_2 produces a higher flux of cold neutrons at 1 meV than sD_2O . Together with the other gain factors, such as an increased production volume and optimized moderator geometries, a production rate of 1.4 to 1.6×10^7 UCN/s is expected [21].

3 Highlights of recent progress

3.1 Construction and tests of the helium cryostat for the new UCN source

As mentioned in Sec. 2.3, the helium cryostat is one of the crucial ingredients of the new UCN source. A highly-efficient 3He - 4He cryostat with a cooling power of 10 W at ~ 1 K was developed, which enables UCN production with a $40 \mu A$ beam current. The cryostat mainly consists of seven types of heat-exchangers. Its central item is a copper heat exchanger named HEX1, which interfaces between a 0.8 K 3He pot and the UCN production volume filled with He-II. The heat load is removed by latent heat loss due to nucleate boiling of 3He in HEX1. The other heat exchangers are designed to efficiently recover the enthalpy of outgoing fluid at each temperature stage [22, 23]. The construction of the cryostat components commenced in 2019. As they were built, performance of each heat exchanger was characterized by cryogenic tests to validate thermal calculations and simulations used for the design [23]. From September 2020 to March 2021, the full cryostat assembly was tested with natural helium at KEK (Fig. 6). It showed excellent performance in pre-cooling efficiency and its low static heat load. The lowest temperature achieved with 4He was 1.23 K, corresponding to 0.65 K for 3He at the same saturation vapour pressure. In total four cool downs were performed to characterize boiling heat transfer of 4He with different geometries and supply configurations of HEX1 prototypes. Based on these results, the final model of HEX1 is under development. The cryostat was transported to TRIUMF in August 2021. It will be tested with 3He and high-capacity pumps prior to the commissioning with the other parts of the UCN source.

3.2 Magnetic field measurements and simulations for the installation of the magnetically shielded room

One of the most crucial systematic effects which should be controlled for the nEDM measurement is the magnetic field. In deriving Eq. (3), the magnetic fields between the two field configurations ($\uparrow\uparrow$) and ($\uparrow\downarrow$) are assumed to be identical. However, in the actual measurement, variations and inhomogeneities of the magnetic field impose systematic limitations on the measurement. Regarding the magnetic-field stability, the cycle-to-cycle magnetic field stability on the order of 10 fT/cycle is required for an nEDM measurement with the target sensitivity. This will be achieved by a high-performance magnetic shield and correction of magnetic-field variations by the use of a ^{199}Hg co-magnetometer [24]. The magnetic-field fluctuations inside the magnetic shield are required to be on the order of 1 pT/cycle. To meet this requirement, a magnetically shielded room (MSR) consisting of four layers of mumetal has been designed (Fig. 5). The design shielding factor on the order of 10^5 is validated by finite-element-analysis (FEA) simulations. In addition, the residual magnetic field and its gradient in the central $1 \times 1 \times 1 \text{ m}^3$ volume will be $< 1 \text{ nT}$ and 100 pT/m , respectively.

Although such magnetic shields have been developed and tested at other facilities [25, 26], a unique challenge in case of TUCAN results from a strong background field up to $|\mathbf{B}| \approx 370 \mu\text{T}$ from the TRIUMF cyclotron. This induces a magnetic flux in the outermost layer of the MSR on a level close to the saturation induction of mumetal, which is about 700 mT. To characterize the spatial distribution of the background magnetic field, three-dimensional magnetic field mapping was performed around the planned installation location of the MSR in August 2019 (when the cyclotron was operational) and February 2020 (during cyclotron shutdown) (Fig. 7a). Fig. 7b and c show the spatial distributions of the vertical component of the background magnetic field when the cyclotron was operated. The main part of the background field is approximated by a dipole field originating from the cyclotron. Based on this data, a set of compensation coils are designed, which will reduce the magnetic flux in the mumetal layer and ensure the performance of the MSR in the presence of the background field. Results of FEA simulations shown in Fig. 8 demonstrate that sufficient compensation can be achieved by a simple combination of square coils. The MSR and the compensation coil system will be installed by November 2022. Thereafter, installation and tests of inner coils and magnetometers in the MSR will begin.

3.3 Component tests with cold and ultracold neutrons at J-PARC/MLF

Some components of the new UCN source and the nEDM spectrometer have been developed by the use of cold and ultracold neutrons available at the Materials and Life Science Facility (MLF) of J-PARC. The beamline BL05 [27] of the MLF is equipped with a Doppler-shifter-type UCN source, which produces pulsed UCNs by decelerating very cold neutrons (kinetic energies of $\sim 100 \mu\text{eV}$) with a rotating neutron mirror moving backwards in respect to the incident neutrons [28].

In June 2020, a systematic measurement was conducted to characterize UCN transmission through cylindrical guides coated with Nickel phosphorus (NiP). The transmission rate of UCNs through a guide was measured for different incident angles. By comparing the measured transmission to Monte-Carlo simulations, a realistic model of diffuse reflection of UCNs due to surface roughness of the guide was developed [29].

The pulsed UCNs from the Doppler shifter can also be used to test storage lifetime of critical inner components. A pilot experiment was successfully performed in February 2021, where a one-meter UCN guide was used as a storage volume [29]. A storage experiment of a prototype of the EDM measurement cell (Fig. 5) is planned in spring 2022.

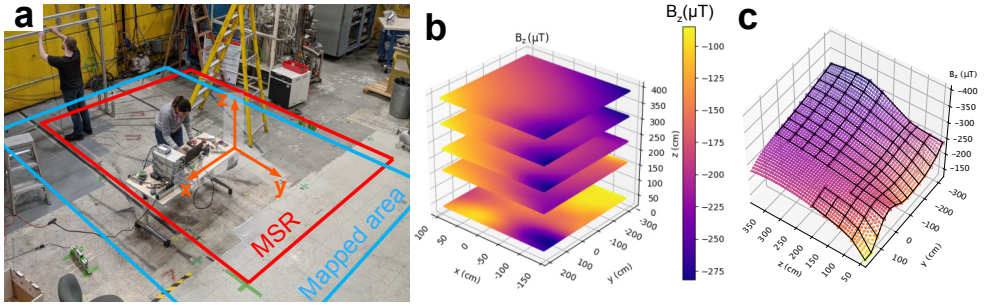


Figure 7. **a.** Magnetic field mapping campaign performed at the planned location of the TUCAN MSR in the TRIUMF Meson Hall. The mapped area, the planned location of the MSR, and the coordinate system are indicated in the photograph. **b.** The magnetic field distribution obtained by the measurement when the cyclotron was operational. The three-dimensional distribution of the vertical component B_z is displayed. **c.** A two-dimensional cut of the data of **b.** at a plane $x = 182$ cm. The data points connected with solid black lines are those obtained by actual measurements. Data indicated by the coloured dots are obtained by interpolating the measured data points. Some local field distributions are observed near the floor height $z = 0$. The field distribution at high z positions is found to be approximated by a dipole field originated from the TRIUMF cyclotron, which is located in $-x$ direction in this coordinate system.

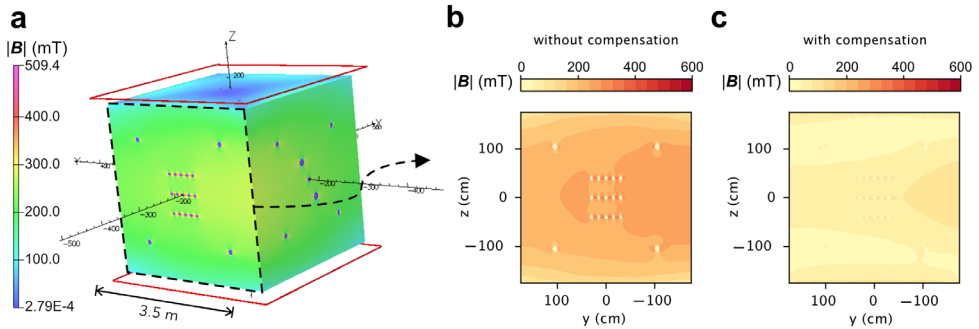


Figure 8. Results of finite-element magnetic field simulations for design of the compensation coil system surrounding the MSR. **a.** The MSR and the coils are placed in a background magnetic field reproduced from an actual magnetic field map. The scale indicates the norm of the in-plane magnetic flux density $|\mathbf{B}|$ of the outermost layer of the mu-metal sheet when the coils are not charged. **b.** The $|\mathbf{B}|$ distribution in one of the planes when the coils are not charged. Around the holes of the mumetal plates, it reaches up to $|\mathbf{B}| \approx 500$ mT. **c.** The $|\mathbf{B}|$ distribution in the same plane when the upper and lower coils are charged to 1000 Ampere-turns. The in-plane flux density $|\mathbf{B}|$ is reduced to about 100 mT or less.

Another item under development is the UCN spin analyzer, whose main component is a thin iron film magnetized by a surrounding magnet. When a UCN traverses the film, it experiences a spin-dependent potential expressed as

$$V_{\uparrow,\downarrow} = V_F \pm \mu_n \cdot B \approx 209 \mp 60 \text{ neV/T} \cdot B, \quad (5)$$

where $\mu_n \approx -60 \text{ neV/T}$ and $V_F \approx 209 \text{ neV}$ represent the magnetic moment of the neutron and the Fermi potential of iron, respectively. Because kinetic energies of UCNs are $\lesssim 300 \text{ neV}$, a magnetic flux density $B \approx 2 \text{ T}$ produced in a fully saturated iron film makes it a filter which selectively transmits one of the spin components. Iron thin films used for this purpose are required to be saturated with a small ($\sim 10 \text{ mT}$) magnetic field, and have a saturation induction close to 2 T. The ion-beam sputtering (IBS) facility at the Institute for Integrated Radiation

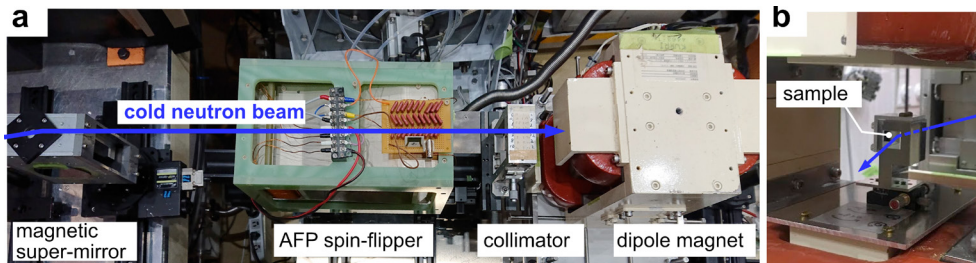


Figure 9. Setup of the cold-neutron reflectometry measurement of iron thin film samples. **a.** The main components of the setup. The cold neutron beam is polarized by a magnetic super-mirror and goes through an AFP spin flipper and a collimator and then injected on a sample placed in a dipole magnet. The neutrons are detected by a two-dimensional detector based on resistor type photomultiplier tubes (RPMT) placed 67 cm downstream of the dipole magnet (not shown in the picture). **b.** View of the dipole magnet from the downstream side. A $20 \times 30 \text{ mm}^2$ sample of silicon substrate iron film is installed in a holder and placed in the magnet.

and Nuclear Science, Kyoto University (KURNS) [30] was used to produce magnetically soft iron thin films on silicon or aluminum substrates. In July 2021, samples of silicon-substrate iron thin films were characterized by a cold-neutron reflectometry measurement on the low-divergence beam branch of BL05 [27]. In this method, neutrons are injected on a surface of a sample with a small incident angle to obtain the reflectivity as a function of the wavevector transfer $R(q)$. The Fermi potential of the sample is obtained from the critical wavevector transfer q_c , below which the neutrons are totally reflected. In this experiment, the incident neutrons are polarized by a magnetic super-mirror [31] and injected on a sample placed in a magnetic field of a dipole magnet (Fig. 9). A spin flipper based on the principle of adiabatic free passage [32] is placed between the super-mirror and the dipole magnet to flip the neutron spin when activated. By measuring the reflectivity for each spin component under different magnetic fields, the effective potential $V_{\uparrow,\downarrow}$ of Eq. (5) is extracted. Samples with different iron-layer thicknesses (30, 50, 90 nm) are measured under a magnetic field of 0–8 mT. From the result, the effective potential $V_{\downarrow} \approx 328 \text{ neV}$ (corresponding to $\approx 2.0 \text{ T}$ magnetic flux density) is obtained with a few mT of the applied field. As the next step, a polarization experiment of pulsed UCNs provided by the Doppler shifter is planned in spring 2022.

4 Conclusions and outlook

The measurement of the nEDM provides a direct test of time-reversal violation and provides constraints on the BSM theories. The TUCAN collaboration aims to measure the nEDM with $10^{-27} e \cdot \text{cm}$ precision to provide an order-of-magnitude improvement upon the current best experimental limit. To overcome the statistical limitation of the current nEDM measurement with stored UCNs, TUCAN is developing a new high-intensity UCN source based on spallation neutron production and the super-thermal UCN conversion with He-II.

There has been major progress on the core components of the new UCN source and the nEDM spectrometer. Among them, the status of the helium cryostat, magnetic-field subsystems including the MSR, and component tests using at J-PARC/MLF have been reported.

Currently, we aim to install the major part of the new UCN source on the TRIUMF beam-line by October 2022, and to start commissioning the nEDM spectrometer in 2023.

Acknowledgements

The author thanks C. Marshall, T. Hessels, S. Horn and D. Rompen (TRIUMF) for their engineering support, M. Hino (KURNS) for iron thin film production and valued support on the cold-neutron reflectometry measurement.

The neutron experiments at the Materials and Life Science Experimental Facility of J-PARC were performed under S-type project of KEK (Proposal No. 2019S03). The iron thin film fabrication work has been carried out under the visiting Researcher's Program of the Institute for Integrated Radiation and Nuclear Science, Kyoto University.

The work of the TUCAN collaboration is supported by the Canada Foundation for Innovation (CFI), the Canada Research Chairs program, the Natural Sciences and Engineering Research Council of Canada (NSERC), B.C. Knowledge Development Fund (BCKDF), Research Manitoba, the Japan Society for the Promotion of Science (JSPS), Yamada Science Foundation, and the RCNP Collaboration Research network (COREnet) program.

References

- [1] T. D. Lee and C. N. Yang, *Phys. Rev.* **104**, 254 (1956); *Phys. Rev.* **106**, 1371 (1957).
- [2] C. S. Wu et al., *Phys. Rev.* **105**, 1413 (1957).
- [3] A. D. Sakharov, *Pisma Zh. Eksp. Theor. Fiz.* **5**, 32 (1967).
- [4] L. Canetti, M. Drewes and M. Shaposhnikov, *New. J. Phys.* **14**, 095012 (2012).
- [5] P. A. R. Ade et al. [Planck Collaboration], *Astron. Astrophys.* **594**, A13 (2016).
- [6] R. Aaij et al. [LHCb Collaboration], *Phys. Rev. Lett.* **124**, 03801 (2020).
- [7] The T2K Collaboration, *Nature* **580**, 339 (2020).
- [8] T. E. Chupp et al., *Rev. Mod. Phys.* **91**, 015001 (2019).
- [9] G. Lüders, *Ann. Phys.* **2**, 1, (1957).
- [10] J. Engel, M. J. Ramsey-Musolf and U. van Kolck, *Prog. Part. Nucl. Phys.* **71**, 21 (2013).
- [11] J. M. Pendlebury and E. A. Hinds, *Nucl. Inst. Meth. A*, **440**, 471 (2000).
- [12] J. H. Smith, E. M. Purcell, and N. F. Ramsey, *Phys. Rev.* **108**, 120 (1957).
- [13] W. B. Dress et al., *Phys. Rev. D* **15**, 9 (1977).
- [14] C. Abel et al., *Phys. Rev. Lett.* **124**, 081803 (2020).
- [15] N. F. Ramsey, *Phys. Rev.* **78**, 69 (1950).
- [16] S. Kawasaki, T. Kikawa and R. Matsumiya, *High Energy News (KEK)* **37**, 11 (2018).
- [17] R. J. Donnelly and C. F. Barenghi, *J. Phys. Chem. Ref. Data* **27**, 1217 (1998).
- [18] S. Ahmed et al. [TUCAN Collaboration], *Phys. Rev. C* **99**, 025503 (2019).
- [19] Y. Masuda et al., *Phys. Rev. Lett.*, **108**, 134801 (2012).
- [20] R. Golub and J. M. Pendlebury, *Phys. Lett.* **62A**, 337 (1977).
- [21] W. Schreyer et al., *Nucl. Inst. Meth. A* **959**, 163525 (2020).
- [22] S. Kawasaki et al., *IOP Conf. Ser.: Mater. Sci. Eng.* **755**, 012140 (2020).
- [23] T. Okamura et al., *IOP Conf. Ser.: Mater. Sci. Eng.* **755**, 012141 (2020).
- [24] K. Green et al., *Nucl. Inst. Meth. A* **404**, 381 (1998).
- [25] I. Altarev et al., *J. App. Phys.* **117**, 183903 (2015).
- [26] S. Knappe-Grueneberg et al., *J. App. Phys.* **103**, 07E925 (2008).
- [27] K. Mishima et al., *Nucl. Inst. Meth. A* **600**, 342 (2009).
- [28] S. Imajo et al., *Prog. Theor. Exp. Phys.* **2016**, 013C22 (2016).
- [29] T. Higuchi, S. Imajo et al., Annual report of Research Center for Nuclear Physics, Osaka University 2020 (2021).
- [30] M. Hino et al., *Nucl. Inst. Meth. A* **797**, 265 (2015).

- [31] M. Hino et al., *Physica B* **385-386**, 1187 (2006).
- [32] S. V. Grigoriev, A. I. Okorokov and V. V. Runov, *Nucl. Inst. Meth. A* **384**, 451 (1997).